Article:
Liang, G, Zeng, Y, Hu, X et al. (7 more authors) (2017) Monolithic semiconductor lasers with dynamically tunable linear-to-circular polarization. ACS Photonics, 4 (3). pp. 517-524. ISSN 2330-4022

https://doi.org/10.1021/acsphotonics.6b00703

Monolithic semiconductor lasers with dynamically tunable linear-to-circular polarization

Guozhen Liang,[1] Yongquan Zeng,[1] Xiaonan Hu,[1] Hao Yu,[1] Houkun Liang[2], Ying Zhang[2],

Lianhe Li,[3] Alexander Giles Davies,[3] Edmund H. Linfield,[3] Qi Jie Wang[1,*]

[1] *Center for OptoElectronics and Biophotonics, School of Electrical and Electronic Engineering & The Photonics Institute, Nanyang Technological University, 50 Nanyang Avenue, 639798 Singapore.*

[2]*Singapore Institute of Manufacturing Technology, 71 Nanyang Drive, 638075 Singapore.*

[3]*School of Electronic and Electrical Engineering, University of Leeds, Leeds LS2 9JT, UK.*

Emails:

Guozhen Liang : gzliang@ntu.edu.sg

Yongquan Zeng : ZENG0075@e.ntu.edu.sg

Xiaonan Hu: HUXI0011@e.ntu.edu.sg

Hao Yu: haoyu@ntu.edu.sg

Houkun Liang: hkliang@simtech.a-star.edu.sg

Ying Zhang: yzhang@simtech.a-star.edu.sg

Lianhe Li: L.H.Li@leeds.ac.uk

Alexander Giles Davies: G.Davies@leeds.ac.uk

Edmund H. Linfield: E.H.Linfield@leeds.ac.uk

Qi Jie Wang : qjwang@ntu.edu.sg

*Contact details of corresponding author :

Assoc. Prof. Qi Jie Wang

Center Director, Photonics Center of Excellence

School of Electrical and Electronic Engineering & School of Physical and Mathematical Sciences,

Nanyang Technological University

50 Nanyang Ave, 639798, Singapore

Phone: (65) 6790 5431, Fax: (65) 6792 0415, Email : qjwang@ntu.edu.sg

Office: S2-B2b-74A

Abstract

The ability to control the polarization state of emission from semiconductor lasers is essential for many applications in spectroscopy, imaging, and communications, *inter alia*, with monolithic integration approaches being extremely beneficial. Although manipulating the output polarization of radiation from a laser can be achieved through a number of approaches, obtaining continuous *dynamic* control, e.g. from linear to circular, remains extremely challenging. In this paper, we demonstrate that the polarization of terahertz (THz) frequency radiation can be continuously tuned electronically from linear to circular polarization by monolithically integrating in-plane metasurfaces with two phase-locked semiconductor-based THz quantum cascade lasers (QCLs). Moreover, the metasurfaces – metal antenna arrays in this case – also act as efficient beam collimators, yielding a collimated beam divergence of ~ 10° × 10°. Our results, however, have broad applicability to a wide range of semiconductor lasers operating from the visible to THz regions of the electromagnetic spectrum.

Keywords: tunable polarization; semiconductor laser; terahertz quantum cascade laser; metasurface; high collimation

INTRODUCTION

The ability to manipulate the polarization states of radiation has a breadth of applications across the electromagnetic spectrum. For example: in communication systems, polarization multiplexing/diversity[1–4] can significantly improve data reliability and transmission rate, based on which the Optical Internetworking Forum has proposed a scheme to reach 100 Gb/s per channel over existing infrastructure[5]; in spectroscopy and sensing applications, variable polarization of the light source is an attractive feature for investigating materials with local symmetry, e.g., molecular chirality[6,7]; in optical holography, circularly polarized beams make it possible to realize wide-angle holograms with 80% power efficiency over a broad wavelength range, upon illuminating metallic nanorod arrays[8]; and, continuously tunable linear-elliptical polarization significantly simplifies the design of ellipsometry systems, by eliminating the use of Soleil-Babinet compensators or rotating analyzers[9].

Manipulation of the polarization state of light usually relies on external, bulky, optical components, such as wave plates and polarizers. However, these do not lead to system miniaturization and fast operation, and many such components are lossy over specific wavelength ranges (e.g., marketed terahertz (THz) frequency continuous polarization converters have a transmission < 30%)[10]. Therefore, there is an essential need to develop low loss, monolithic devices with controllable polarization. Previously, it is has been demonstrated that the polarization state of spin-polarized lasers[11] and light-emitting diodes[12] can be tuned by varying the amplitude or direction of an applied external magnetic field, achieving a degree-of-circular-polarization (DOCP) of up to 50%. Furthermore, a DOCP of

98% was achieved in quantum cascade lasers (QCLs) with built-in antennas[13,14] for selected far-field regions of the emission, albeit pre-determined by the device fabrication process. However, monolithic light sources have yet to be demonstrated in which electronic tuning leads to a widely and dynamically tunable polarization state, and a high DOCP.

MATERIALS AND METHODS

Elliptically or circularly polarized light can be treated as the superposition of two orthogonally polarized components with a $\pi/2$ phase difference. Therefore, if the amplitude of each component can be tuned independently, the polarization of the resultant field will evolve continuously from linear to circular polarization. In this work, as a proof-of-principle, we implement this strategy with THz frequency QCLs[15–17]; these electrically pumped, semiconductor-based THz sources offer great potential for many diverse applications, including spectroscopic sensing[18,19] and non-invasive detection[20–23]. First, we designed a dielectric-loaded THz surface plasmon (SP) waveguide to provide a flexible platform for THz QCL beam manipulation. Then, to control the polarization of the beam, a metallic subwavelength scattering antenna array, a so-called metasurface[24–26], was integrated onto the SP waveguide. Subsequently, two QCLs were phase-locked, but with cross-polarized beams that had a phase shift of $\sim\pi/2$. The intensity of each beam could be controlled relatively independently, enabling the polarization of the overlapping beam to be tuned continuously from linear to near-circular. Moreover, the metallic antenna array also acted as an efficient beam collimator, yielding a small beam divergence of $\sim 10° \times 10°$.

Design of an integrated THz dielectric-loaded surface plasmon (DLSP) waveguide

Surface plasmons have underpinned a breadth of studies at short wavelengths (from the visible to the mid-infrared) owing to their capability for confining and manipulating optical waves on a subwavelength scale[27–30]. However, in the THz region, a flat metal surface cannot support confined SPs because of the negligible penetration depth of the THz wave into the metal[31]. To confine THz wave onto a metal surface, previous work has therefore used subwavelength-structured metal surfaces, which support 'spoof' SPs in the same way that a flat metal surface supports SPs in the short wavelength range[32–35]. However, given their complexity in design and fabrication, such subwavelength-structured metal surfaces are not easily integrated with optoelectronic devices, or combined with other optical functionalities.

In this paper, we demonstrate a DLSP waveguide for the confinement and propagation of THz waves on a flat surface. This is much simpler, in both design and fabrication, than using a structured metal surface, as it comprises simply a GaAs coated metal layer (Figure 1a). In our device, the GaAs layer is actually the QCL active region itself, which simplifies the device fabrication even further, as no additional material growth is required. By correct choice of the thickness of the GaAs layer, the THz electric field can then be confined at the GaAs-air interface, with little field residing in the GaAs layer (Figure 1b), leading to a low propagation loss in the waveguide being achieved. Figure 1b also shows the efficient coupling of the THz wave (free-space wavelength λ_0 = 96 μm) emanating from the QCL (with a double-metal waveguide) to the integrated DLSP waveguide. Note that the THz wave is strongly confined to the GaAs surface with an evanescent tail of only ~30 μm penetrating into the air, with the

electric field profile along the white dashed line depicted by the red curve. As a comparison, Figure 1c and 1d give a schematic illustration of the device, and plot of electric field distribution when there is no GaAs DLSP waveguide. No bound surface wave is observed on the metal surface.

The variation of propagation length and coupling efficiency of the THz emission from the QCL into the DLSP waveguide was calculated as a function of the GaAs thickness (Figure 1e). For the GaAs layer, which is actually part of the QCL active region itself, a refractive index of 3.5 and a material loss of 11 cm^{-1} was used (corresponding to an average doping of 5×10^{15} cm^{-3})[36]. The complex refractive index of the metal (gold in devices presented in this paper) was calculated to be 238 + 552*i* using the Drude–Lorentz approximation[37], which agrees well with the measured result in Ref. 38. The thicker the GaAs layer, the higher the coupling efficiency of the light from the QCL to the DLSP, but this is accompanied by a larger waveguide loss and thus a shorter propagation length. In the design, we chose a GaAs thickness of 5 μm to maintain a high coupling efficiency (55%) while simultaneously allowing a reasonable propagation length (3.3 mm). From a more intuitive point of view, in the DLSP waveguide, the metal and the thin (compared to the wavelength) GaAs layer constitute an effective medium for THz waves, with an average concentration of electrons that is reduced so that the THz wave can penetrate more easily into the medium. This leads to a larger effective refractive index ($n_{eff}=1.13$ in our case), thereby rendering the THz field bound onto the interface, which is reflected by the short evanescent tail, which is given by $\lambda_0/\left(2\pi\sqrt{n_{eff}^2-1}\right)$. A larger n_{eff} reduces the impedance mismatch of the electromagnetic wave between the metal-metal waveguide of QCL and the outer DLSP waveguide, leading to

a higher coupling efficiency of the THz wave from QCL to the DLSP waveguide, as well as a higher output power. Simulations show that the presence of the DLSP increases the output power by approximately 40%.

Metasurfaces for output polarization control of THz QCLs

Subwavelength metallic antennas were incorporated into the DLSP waveguide, as illustrated in Figure 2a and b. Each antenna is excited by an SP plane wave generated from a THz QCL, and will have electrons oscillating along the antenna length. The resultant oscillating electric dipoles will emit THz radiation polarized in the same direction (Figure 2c). In contrast to the cases in Ref. 13 and 39, where slot antennas drilled on a metal film were used as a polarization-sensitive element, our strip-type antenna responds to, and re-emits, the electric field component parallel to its elongation. This is because the slot and strip antennas are complementary, with their electric and magnetic fields interchanged — the slot antenna generates a magnetic dipole oriented along the slot with an induced electric field orthogonal to the slot.

To produce a narrow directional THz beam from a set of antennas, they are arranged into an array and form a second-order grating with a period of 80 μm. The constructive interference of the THz radiation from each antenna leads to a collimated beam pointing normal to the surface. The dimensions of each antenna are 21 μm × 3 μm × 0.4 μm, and the lateral separation is 37 μm – subwavelength so as not to introduce diffraction, but large enough to avoid coupling between neighbouring sites (the detailed selection of these dimensions is given in Supplementary Information). To strengthen the scattering effect of the

antennas, they are placed on top of 5-μm-high GaAs pedestals (fabricated by patterning the QCL active region) (Figure 2b). Figure 2d shows the scattering effect of the antenna placed at different positions. The existence of the GaAs pedestal greatly enhances the antenna scattering owing to it acting as a dielectric antenna. Without the GaAs pedestal, an antenna 5 μm above the DLSP waveguide shows no significant difference in scattering strength compared with an antenna placed directly on the waveguide surface.

Phase locking of the THz QCLs

The antenna structure is fed by a tapered THz QCL, as shown in Figure 3a. The taper is designed to collimate the emitted beam in the lateral direction, whilst simultaneously amplifying the power. For such a large tapering angle (36^{o}), a flat output facet is not suitable as it will distort the emitted beam owing to the large mismatch between the wavefront radiated from the ridge segment, and the shape of the facet. Therefore, it is designed to be an arc centered 20 μm below the taper-ridge interface[31]. Figure 3b and 3c show the electric field distribution of the emission from the tapered THz QCL – laterally collimated output beams can be observed.

A half racetrack waveguide structure is used to phase lock the left and right THz QCLs so that the emissions from the two QCLs are in phase (or, phase-shifted by π)[40,41]. The half racetrack section is electrically insulated from the QCL by etching down to the bottom of the active region using inductively coupled plasma (ICP) etching, and forming a gap. The width of the gap should be chosen such that the two lasers are not so strongly coupled that independent control of the intensity from each laser becomes impossible, but narrow enough

to ensure phase locking, and to minimize undesired scattering of THz emission into the far field. The best tradeoff was a gap of 20 μm, as determined by simulations with COMSOL Multiphysics, a commercial finite-element-method solver. This fixed phase relation is achieved by injecting a portion of the output light from one laser (master) into the other (slave), which have an eigenfrequency the same as (or very close to) the frequency of the injecting light. Since the injection can be seen as an additional gain to the slave laser, the optical mode of the slave laser with the same frequency will be excited, even if it was originally operating at other modes/frequencies. In our case, as the injection of light is bi-directional, the phase-locking can be understood in the framework of mutual injection locking[42,43]. On the other hand, it can also be interpreted as weakly coupled cavities. The coupling is weak because the power reflection at the back facet by the gap is ~60% due to the strong subwavelength vertical confinement by the two metal, and only <10% of the incident light is coupled into the half racetrack structure. Therefore, if the half racetrack is transparent (without either gain or loss), less than 1% of the light from one laser is coupled to the other (see Fig. S3 in Supplementary Information for details). In our polarization measurements below, the half racetrack structure was biased at 0.53 A, which is near the transparent point. Figure 3b shows the simulated electric field distribution in the device when only the right hand side QCL is electrically pumped, whilst Figure 3c shows the situation when both QCLs, as well as the half racetrack structure, are pumped simultaneously, but with different injection currents. The phase locking scheme allows relatively independent control of the intensity from each QCL (see Fig. S4 in Supplementary Information for details).

The two sets of antennas (left and right) are cross oriented, and vertically shifted by 21 μm (see Figure 3a), around one quarter of the SP wavelength (85 μm). This introduces a ~π/2 phase difference in the excitation of the two antenna arrays, which are also cross polarized. If the emission direction of the device is normal to the surface (as it is), no additional phase difference will be accumulated during free-space propagation of THz waves, the phase difference in the excitation of the two antenna arrays will be mirrored in their emissions in the far field. This is opposite to the case in Ref. 13, where the antennas are excited in phase and the required phase shift is accumulated during free-space propagation owing to the tilted emission angle with respect to the surface normal.

Device fabrication

As illustrated in Fig. S6 in Supplementary Information, fabrication of the device started with Au-Au thermo-compression bonding of the QCL active region onto an n+ GaAs receptor wafer. The original QCL substrate was then removed by a combination of lapping and selective chemical etching, leaving a 10-μm-thick active region. The top contact of the QCLs, the half racetrack, and rectangles covering the whole antenna areas, were next defined by conventional optical lithography and lift-off of a Ti/Au/Ti (15 nm/350 nm/10 nm) layer. The additional 10 nm Ti layer was employed to allow firm adherence of a subsequently-grown SiO_2 film onto the metal surface. The SiO_2 was deposited by PECVD and patterned into the shape of the QCLs, half racetrack and antennas using optical lithography and reactive-ion etching (RIE) with an O_2 and CF_4 gas mixture. The antennas were then defined by wet etching away the exposed metal layer in the SP waveguide region using a diluted HF solution

and gold etchant. The sample was subsequently etched by ICP to a depth of 5 μm with the patterned SiO_2 as the mask using an Ar, Cl_2 and BCl_3 gas mixture. The whole SP waveguide region was next covered by a thick photoresist and patterned, and a second ICP etching was performed to etch the active region outside the SP waveguide region, the half racetrack, and the QCL mesas down to the bottom metal layer. The thick photoresist was removed by acetone, and a further RIE etch removed the SiO_2 mask and the underlying adhesive Ti layer. Finally, the substrate was thinned to 120 μm and a 20/300 nm Ti/Au layer was deposited to form the bottom contact. The samples were cleaved, indium-mounted on Cu submounts, wire-bonded, and finally attached to the cold finger of a cryostat for measurement.

RESUTLS AND DISCUSSIONS

Far-field investigation of the phase-locked device

The device was operated at 10 K under pulse excitation with 10 kHz, 500 ns electric pulses (light-current-voltage characteristics and spectra of the QCL are provided in Supplementary Information). Two-dimensional far-field emission patterns were measured by scanning a pyroelectric detector on a spherical surface 15 cm away from the emission area. The results are presented in Figure 4. The (0, 0) point in the far-field pattern corresponds to the direction normal to the device surface. Also shown are the calculated results obtained by a full-wave finite-difference time-domain (FDTD) method implemented in the commercial simulation package Lumerical FDTD, which reproduce the main features of the measured patterns. Figure 4a shows the far-field pattern with only the left QCL biased (the red part in the inset).

It exhibits a ~13°×9° (full-width-at-half-maximum (FWHM)) elliptical spot, tilted in the orientation of the antennas. To better understand the formation of this beam, we investigated the near field distribution of the device. As is shown in Figure 4e, the antennas tend to deflect the SP wave towards the direction perpendicular to their length. This is because an electric dipole radiates strongest along the perpendicular bisector of its length. In addition, it should be noted that without the DLSP waveguide and the antenna structure, the device emits fairly uniformly in the vertical direction with a divergence of ~180°, owing to the strong subwavelength mode confinement in the QCL (given by the fact that the 10-μm-thick active region is sandwiched by two metal plates, whilst the laser wavelength is ~100 μm). Therefore, the antenna structure is functioning as a highly efficient collimator, and the divergence of the emitted beam is diffraction limited. Pumping the laser with a higher current will give rise to extra emissions at a higher frequency (Supplementary Information); however, with the half racetrack active, the emission peaks in the spectrum can be reduced to a single peak (case (b) in Figure 4d). This phenomenon can be understood as the Vernier effect in coupled cavities[44,45] (Supplementary Information). As the frequency increases, the corresponding far-field pattern shifts upwards (Figure 4b).

When the whole device is pumped electrically, the far-field pattern appears as a superposition of the patterns of the left and right devices individually (Figure 4c). However, although the biasing conditions of each individual part are the same as that in Figure 4a and 4b, the far-field pattern in Figure 4c is not simply the superposition of Figure 4a and 4b. Similarly, instead of having two peaks corresponding to the separate lasers in the cases of Figure 4a and 4b, the spectrum for the case of Figure 4c has a main peak at a slightly lower

frequency (Figure 4d). This indicates that the left and right devices are phase-locked by the half racetrack structure, and their combined emission is coherent – the basis for demonstrating a polarization tunable device.

Demonstration of dynamically tunable polarization

The polarization states of the emission were measured by rotating a wire-grid polarizer in front of the detector, which was placed at the intensity maximum of the far-field distribution. Optical power was collected within a half angle of 2.5° (the region enclosed by a black dotted circle in Figure 4f). The collected power accounts for ~15% of the total emission. Figure 5 presents the detected power as a function of the rotation angle (α) of the polarizer in polar plots. α =0° corresponds to the direction along the laser ridge. Figure 5a and b show the results with either the left or the right laser biased, corresponding to the cases in Figure 4a and 4b, respectively. With only one laser on, the radiation in the collected region is excellently linearly-polarized at a predetermined direction, which is consistent with that of the antenna and the far-field patterns. The high cross-polarization ratio demonstrates the high efficacy of our antenna structure to project the polarization of a QCL onto a specific direction. When both lasers, together with the racetrack structure, are electrically pumped, however, elliptical polarization is observed due to the coherent overlap of the two beams. Figure 5c plots the polarization states with the current of the left QCL fixed at 3.49 A whilst changing the current in the right QCL. Figure 5d shows the evolution of the polarization state with the variation of the left pumping current while fixing the right pumping current at 3.67 A. For the black curve in Figure 5d, $I_{max}: I_{min} = 56: 44$. According to the definition of DOCP in Ref. 13, which is

DOCP $= 2 \cdot I_{max}^{1/2} \cdot I_{min}^{1/2}/(I_{max} + I_{min})$, a DOCP value as high as 99% is obtained. This demonstrates that the device is capable of dynamically changing its polarization state from linear to near-circular.

Device without phase shift

To provide further confirmation that the THz beam in the power collection region is truly elliptically polarized, and not just an incoherent mix of two linearly-polarized beams, we fabricated a device without any phase shift between the two sets of antenna arrays (Figure 6a). If the emitted radiation from the two antenna arrays are coherent, their overlap will result in a linearly polarized laser beam, but in a different direction from the emission from the separate arrays (Figure 5a and 5b). Figure 6b plots the experimental results of such a device, showing a variation of linear polarization, which is rotated by changing the currents in the two QCLs independently. The non-zero minimum intensity in the results from the left QCL alone can be attributed to a non-negligible direct emission from the QCL into the power collection region, which could arise from imperfection of the fabricated device, resulting in a larger fraction of the light not being coupled into the SP wave. There may also be a contribution from undesired scattering of the SP wave by damage/dust on the waveguide surface.

The emitted radiation mainly consists of three components: 1) the emission from the left antenna array $A\cos(\omega t+\varphi)(\hat{x}+\hat{y})/\sqrt{2}$; 2) the direct emission/undesired scattering from the left QCL $C\cos(\omega t)\hat{y}$; and 3) the emission from the right antenna array $-B\cos(\omega t+\varphi)(-\hat{x}+\hat{y})/\sqrt{2}$, where A, B and C are electric field amplitudes, $\hat{x}$ and $\hat{y}$ are unit vectors, and φ is the phase difference between the radiation from the antenna arrays and

that directly emitted from the laser facet. The measured intensity as a function of the polarizer angle α is thus given by

$$I(\alpha)=\frac{1}{2}A^2\cos^2(45^\circ-\alpha)+\frac{1}{2}B^2\sin^2(45^\circ-\alpha)+\frac{1}{2}C^2\cos^2(\alpha)$$
$$-\frac{1}{2}AB\cos(2\alpha)+(AC\cos(45^\circ-\alpha)-BC\sin(45^\circ-\alpha))\cos(\alpha)\cos(\varphi).$$

The first three terms correspond to the direct contributions from the three components, and the last three terms are due to interference between these components. The red solid curve in Figure 6c is the fitting of the experimental data with the above equation. If the two arms are not phase-locked, the fourth and last term in the above equation would vanish, meaning there is no interference between A and B, and between B and C. A and C will still have interference, though, as they both originate from the left QCL. The black dashed curve in Figure 6c represents the case without phase locking of the two arms. It deviates from the measured result greatly.

CONCLUSIONS

In summary, we have developed an integrated metasurface structure in which dielectric-loaded plasmonic waveguides are used to couple radiation efficiently from a THz QCL into surface plasmon waves. Subwavelength metasurface antenna arrays are then introduced into the DLSP waveguide to scatter and collimate the SP wave into the direction perpendicular to the waveguide surface, leading to an emitted laser beam with a predetermined polarization state. Moreover, the metasurface antenna structure was also

demonstrated to be a highly efficiently collimator, yielding a beam divergence as narrow as ~13°×9°. We then phase locked two sets of cross-oriented metasurface antenna arrays with a quarter-wavelength shift. By adjusting the emission intensities from each of the two antenna arrays by biasing the corresponding THz QCLs, the polarization of the beam in the overlapping region was dynamically tuned from linear to near-circular polarization, reaching a DOCP as high as 99%. Given the possibility of exciting SP waves on metasurfaces over a wide spectral range, our scheme can also been applied across a broad range of wavelengths, from the THz region of the spectrum through to the near-infrared and visible.

Acknowledgments

This work is supported by (MOE2011-T2-2-147) from Ministry of Education, Singapore, and SERC (grant number 1426500050) from the Agency for Science, Technology and Research (A*STAR), Singapore. L. H. L, A. G. D. and E. H. L. would like to acknowledge the funding support from the Engineering and Physical Sciences Research Council [EP/J017671/1,'COTS']. Support from the Royal Society and Wolfson Foundation is also acknowledged.

Author contributions

G. Z. L. and Q. J. W. conceived the idea. G. Z. L. designed the device. G. Z. L., Y. Q. Z. and X. N. H. fabricated the devices. G. Z. L. carried out the experimental measurements, data analyses, and prepared the figures. L. H. L, A. G. D. and E. H. L. performed the growth of the

QCL active region. G. Z. L. and Q. J. W. wrote the manuscript. A. G. D. and E. H. L. revised the manuscript. H. K. L., Y. Z. and H. Y. improved the manuscript presentation. Q. J. W. supervised the project. All authors reviewed the manuscript.

Additional information

Competing financial interests: The authors declare no competing financial interests

References

1 Barwicz T, Watts MR, Popović M a., Rakich PT, Socci L, Kärtner FX *et al.* Polarization-transparent microphotonic devices in the strong confinement limit. *Nat Photonics* 2007; **1**: 57–60.

2 Fukuda H, Yamada K, Tsuchizawa T, Watanabe T, Shinojima H, Itabashi S-I. Silicon photonic circuit with polarization diversity. *Opt Express* 2008; **16**: 4872–4880.

3 Dong P, Xie C, Buhl LL. Monolithic polarization diversity coherent receiver based on 120-degree optical hybrids on silicon. *Opt Express* 2014; **22**: 2119–2125.

4 Roberts K, O'Sullivan M, Wu KT, Sun H, Awadalla A, Krause DJ *et al.* Performance of dual-polarization QPSK for optical transport systems. *J Light Technol* 2009; **27**: 3546–3559.

5 Optical Internetworking Forum (OIF). 100G long-haul DWDM Framework Document. *Doc OIF-FD-100G-DWDM-010 (June 2009),*; : http://www.oiforum.com/public/impagreements.html.

6 Whitmore L, Wallace B a. Protein secondary structure analyses from circular dichroism spectroscopy: Methods and reference databases. *Biopolymers* 2008; **89**: 392–400.

7 Tang Y, Cohen AE. Enhanced enantioselectivity in excitation of chiral molecules by superchiral light. *Science* 2011; **332**: 333–336.

8 Zheng G, Mühlenbernd H, Kenney M, Li G, Zentgraf T, Zhang S. Metasurface holograms reaching 80% efficiency. *Nat Nanotechnol* 2015; **10**: 308–312.

9 Yoshida H. Optical system for ellipsometry utilizing a circularly polarized probe beam. U.S. Pat. 1997; : 5,619,325.

10 THz Broad-band Phase Transformers. http://www.tydexoptics.com/products/thz_optics/thz_converters/. 2015.

11 Holub M, Shin J, Saha D, Bhattacharya P. Electrical spin injection and threshold reduction in a semiconductor laser. *Phys Rev Lett* 2007; **98**: 1–4.

12 Jiang X, Wang R, Shelby RM, Macfarlane RM, Bank SR, Harris JS *et al.* Highly spin-polarized room-temperature tunnel injector for semiconductor spintronics using MgO(100). *Phys Rev Lett* 2005; **94**: 1–4.

13 Rauter P, Lin J, Genevet P, Khanna SP, Lachab M, Giles Davies a. *et al.* Electrically pumped semiconductor laser with monolithic control of circular polarization. *Proc Natl Acad Sci* 2014; **111**: E5623–E5632.

14 Yu N, Wang QJ, Pflügl C, Diehl L, Capasso F, Edamura T *et al.* Semiconductor lasers with integrated plasmonic polarizers. *Appl Phys Lett* 2009; **94**: 3–5.

15 Köhler R, Tredicucci A, Beltram F, Beere HE, Linfield EH, Davies a G *et al.* Terahertz semiconductor-heterostructure laser. *Nature* 2002; **417**: 156–159.

16 Liang G, Liang H, Zhang Y, Khanna SP, Li L, Giles Davies A *et al.* Single-mode surface-emitting concentric-circular-grating terahertz quantum cascade lasers. *Appl Phys Lett* 2013; **102**: 031119.

17 Kumar S. Recent Progress in Terahertz Quantum Cascade Lasers. *IEEE J Sel Top Quantum Electron* 2011; **17**: 38–47.

18 Federici JF, Schulkin B, Huang F, Gary D, Barat R, Oliveira F *et al.* THz imaging and sensing for security applications—explosives, weapons and drugs. *Semicond Sci Technol* 2005; **20**: S266–S280.

19 Ren Y, Hovenier JN, Higgins R, Gao JR, Klapwijk TM, Shi SC *et al.* High-resolution heterodyne spectroscopy using a tunable quantum cascade laser around 3.5 THz. *Appl Phys Lett* 2011; **98**: 231109.

20 Chan WL, Deibel J, Mittleman DM. Imaging with terahertz radiation. *Reports Prog Phys* 2007; **70**: 1325–1379.

21 Kim SM, Hatami F, Harris JS, Kurian AW, Ford J, King D *et al.* Biomedical terahertz imaging with a quantum cascade laser. *Appl Phys Lett* 2006; **88**: 153903.

22 Lee AWM, Qin Q, Kumar S, Williams BS, Hu Q, Reno JL. Real-time terahertz imaging over a standoff distance (>25 meters). *Appl Phys Lett* 2006; **89**: 4–7.

23 Nguyen KL, Johns ML, Gladden L, Worrall CH, Alexander P, Beere HE *et al.* Three-dimensional imaging with a terahertz quantum cascade laser. *Opt Express* 2006; **14**: 2123–9.

24 Yu N, Genevet P, Kats M a, Aieta F, Tetienne J-P, Capasso F *et al.* Light Propagation with Phase Reflection and Refraction. *Science (80-)* 2011; **334**: 333–337.

25 Ni X, Emani NK, Kildishev a. V., Boltasseva a., Shalaev VM. Broadband Light Bending with Plasmonic Nanoantennas. *Science (80-)* 2012; **335**: 427–427.

26 Yu N, Capasso F. Flat optics with designer metasurfaces. *Nat Mater* 2014; **13**: 139–50.

27 Ebbesen TW, Genet C, Bozhevolnyi SI. Surface-plasmon circuitry. *Phys Today* 2008; **61**: 44–50.

28 Ng B, Wu J, Hanham SM, Fernández-Domínguez AI, Klein N, Liew YF *et al.* Spoof Plasmon Surfaces: A Novel Platform for THz Sensing. *Adv Opt Mater* 2013; **1**: 543–548.

29 Luo X, Ishihara T. Surface plasmon resonant interference nanolithography technique. *Appl Phys Lett* 2004; **84**: 4780.

30 Yu N, Wang Q, Capasso F. Beam engineering of quantum cascade lasers. *Laser Photonics Rev* 2012; **6**: 24–46.

31 Liang G, Dupont E, Fathololoumi S, Wasilewski ZR, Ban D, Liang HK *et al.* Planar integrated metasurfaces for highly-collimated terahertz quantum cascade lasers. *Sci Rep* 2014; **4**: 1–7.

32 Williams CR, Andrews SR, Maier S a., Fernández-Domínguez a. I, Martín-Moreno L, García-Vidal FJ. Highly confined guiding of terahertz surface plasmon polaritons on structured metal surfaces. *Nat Photonics* 2008; **2**: 175–179.

33 Pendry J, Holden A, Stewart W, Youngs I. Extremely low frequency plasmons in metallic mesostructures. *Phys Rev Lett* 1996; **76**: 4773–4776.

34 Navarro-Cía M, Beruete M, Agrafiotis S, Falcone F, Sorolla M, Maier S a. Broadband spoof plasmons and subwavelength electromagnetic energy confinement on ultrathin metafilms. *Opt Express* 2009; **17**: 18184–95.

35 Garcia-Vidal FJ, Martín-Moreno L, Pendry JB. Surfaces with holes in them: new plasmonic metamaterials. *J Opt A Pure Appl Opt* 2005; **7**: S97–S101.

36 Belkin M a, Fan J a, Hormoz S, Capasso F, Khanna SP, Lachab M *et al.* Terahertz quantum cascade lasers with copper metal-metal waveguides operating up to 178 K. *Opt Express* 2008; **16**: 3242–3248.

37 Kohen S, Williams BS, Hu Q. Electromagnetic modeling of terahertz quantum cascade laser waveguides and resonators. *J Appl Phys* 2005; **97**: 053106.

38 Yasuda H, Hosako I. Measurement of terahertz refractive index of metal with terahertz time-domain spectroscopy. *Jpn J Appl Phys* 2008; **47**: 1632–1634.

39 Lin J, Mueller JPB, Wang Q, Yuan G, Antoniou N, Yuan X-C *et al.* Polarization-Controlled Tunable Directional Coupling of Surface Plasmon Polaritons. *Science (80-)* 2013; **340**: 331–334.

40 Kao T-YY, Hu Q, Reno JL. Phase-locked arrays of surface-emitting terahertz quantum-cascade lasers. *Appl Phys Lett* 2010; **96**: 101106.

41 Halioua Y, Xu G, Moumdji S, Li L, Zhu J, Linfield EH *et al.* Phase-locked arrays of surface-emitting graded- photonic-heterostructure terahertz semiconductor lasers. *Opt Express* 2015; **23**: 6915–6923.

42 Chen Z, Hou J, Zhou P, Jiang Z. Mutual Injection-Locking and Coherent Combining of Two Individual Fiber Lasers. *IEEE J Quantum Electron* 2008; **44**: 515–519.

43 Kurtz RM, Pradhan RD, Tun N, Aye TM, Savant GD, Jannson TP *et al.* Mutual injection locking: A new architecture for high-power solid-state laser arrays. *IEEE J Sel Top Quantum Electron* 2005; **11**: 578–585.

44 Höfling S, Heinrich J, Reithmaier JP, Forchel a., Seufert J, Fischer M *et al.* Widely tunable single-mode quantum cascade lasers with two monolithically coupled Fabry-Pérot cavities. *Appl Phys Lett* 2006; **89**: 241126.

45 Kundu I, Dean P, Valavanis A, Chen L, Li L, Cunningham JE *et al.* Discrete Vernier tuning in terahertz quantum cascade lasers using coupled cavities. *Opt Express* 2014; **22**: 16595–16605.

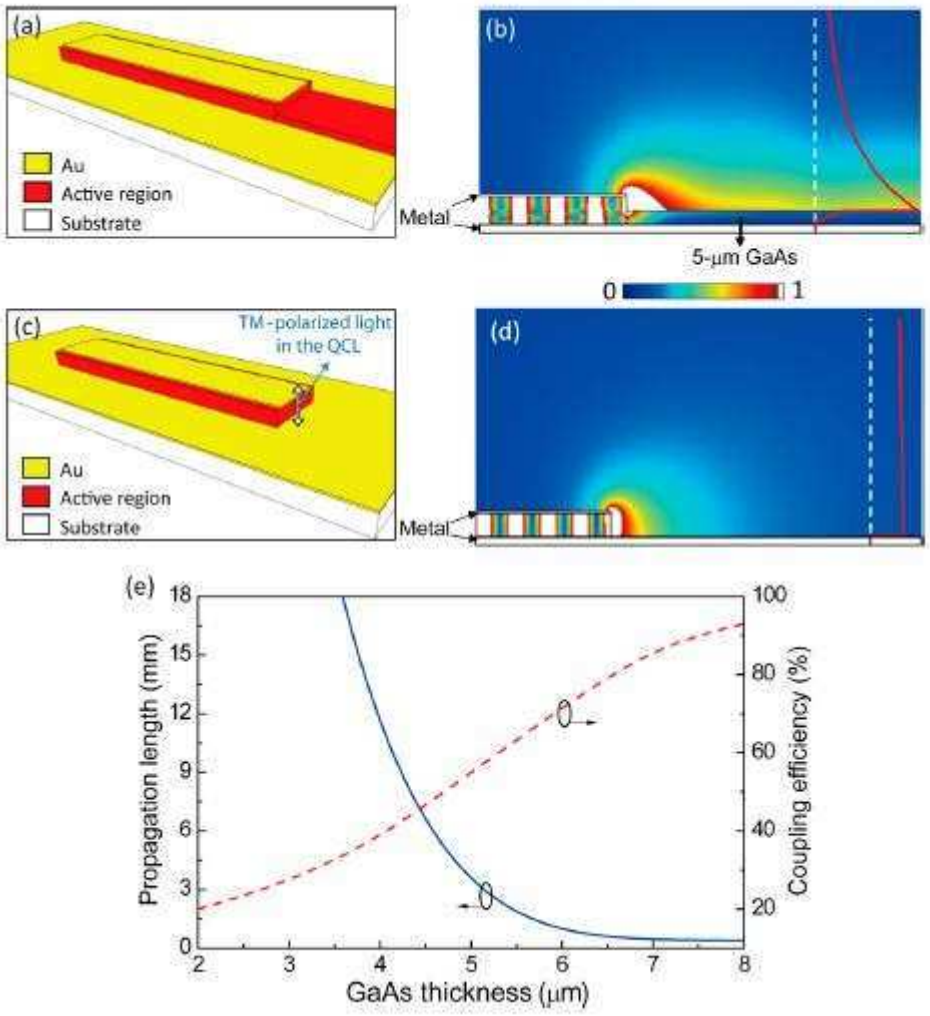

Figure 1. (a) Schematic geometry of a double-metal ridge THz QCL, where the 10-μm-thick active region is sandwiched between two metal plates. The emitted light from the QCL is TM-polarized. (b) Cross-sectional electric field (amplitude) distribution of the THz radiation (λ_0 = 96 μm) near the QCL facet. The electric field profile along the white dashed line is depicted by a red line, indicating no surface plasmon wave. (c) Schematic geometry of the THz QCL with an integrated dielectric-loaded surface plasmon (DLSP) waveguide. (d) Cross-sectional electric field (amplitude) distribution of the device in (c), showing that the THz radiation is coupled from the QCL into the integrated DLSP waveguide, with a coupling efficiency of 55% for a 5 μm thick GaAs layer. The electric field profile along the white dashed line is illustrated by the red curve, and it can be seen that the THz wave is strongly confined to the GaAs surface, with an evanescent tail of 30 μm (λ_0 = 96 μm). Note that the scales of the red lines in (b) and (d) are not the same, the electric amplitude along the white dashed line in (b) is much weaker than that in (d). (e) Calculated propagation length and coupling efficiency of the THz radiation into the DLSP waveguide as a function of the GaAs thickness.

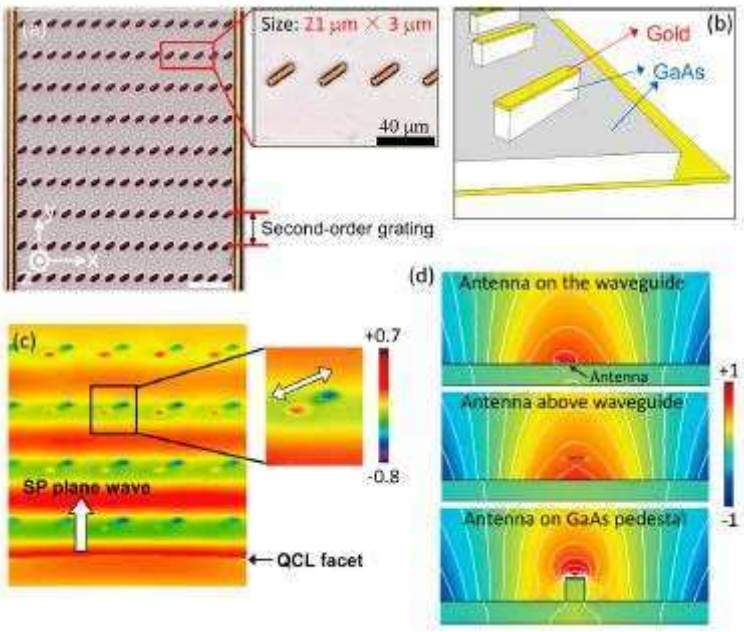

Figure 2. (a) Optical microscope image of the antenna structure (scale bar = 100 μm). The antennas are arranged to form a second-order grating so that a directional output beam can be produced. The dimensions of a single antenna are 21 μm × 3 μm × 0.4 μm. The vertical gold bars at the two sides define the boundaries of the antenna array, and do not affect the operation. (b) Schematic illustration of the structure. The antennas are placed on 5-μm-high GaAs pedestals, formed from the QCL active region. (c) Calculated electric field distribution (E_z) on a plane 2 μm above the antennas. The antennas are excited by the propagating SP plane wave coupled from a THz QCL, resulting in electric dipoles oscillating along the antenna lengths. (d) The scattering effect of the antennas when placed at different positions. The 5-μm-high GaAs pedestal greatly enhances the scattering effect of the antenna on top of it. Plotted in the figure are the E_z distribution (color) and the contour of the E_z field (white lines). The color-coded diagrams are in linear scale.

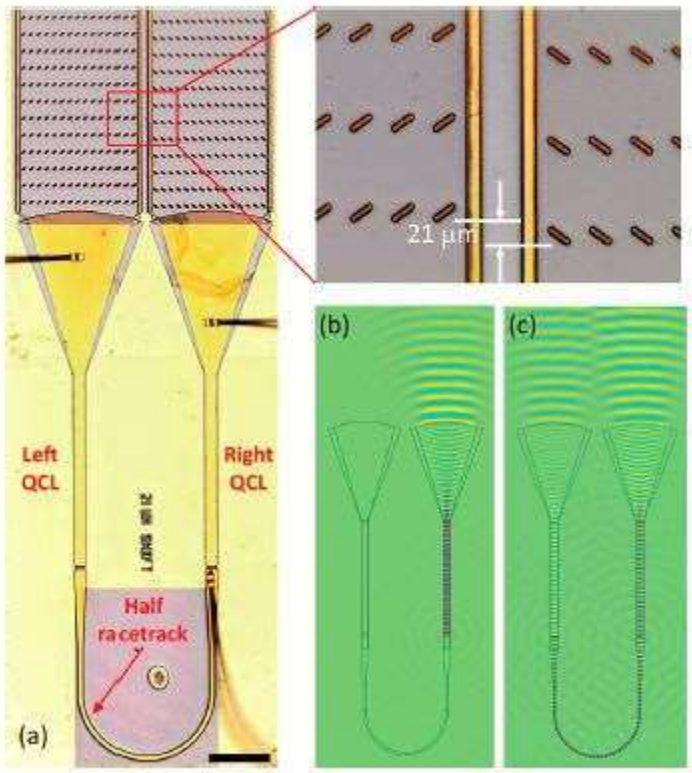

Figure 3. (a) Optical microscope image of a fabricated device. The two sets of antennas are cross oriented and vertically offset by 21 μm, corresponding to a ~π/2 phase shift. The QCL is designed with a tapered structure to collimate THz light in the lateral direction. The left and right QCLs are phase-locked by a half racetrack structure to ensure coherent interference of the radiation from the two antenna arrays. The scale bar is 300 μm long. (b) Simulated electric field distribution in the device when only the right hand QCL is electrically pumped, whilst (c) shows the situation when both QCLs, as well as the half racetrack structure, are pumped simultaneously, but with different injection currents. The phase locking scheme allows relatively independent control of the intensity from each QCL.

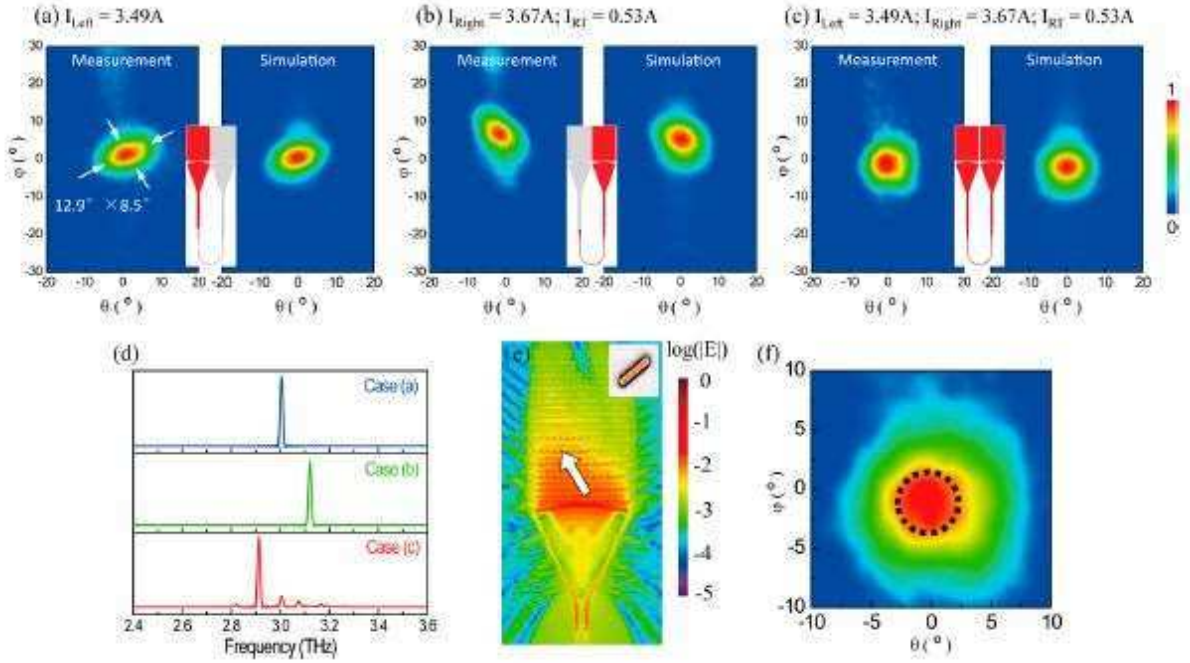

Figure 4. (a) Measured and simulated far-field patterns of the device with only the left QCL pumped using an injection current of I_{left} = 3.49A. (b) Measured and simulated far-field patterns with only the right QCL and the half racetrack structure electrically pumped. The injection currents are 3.67A and 0.53A, respectively. (c) Measured and simulated far-field patterns with all three parts of the structure electrically pumped, the injection currents are I_{left} = 3.49A, I_{right} = 3.67A and I_{RT} = 0.53A. Note that the far-field patterns in this case are not simply the superposition of the far-field patterns in (a) and (b). (d) The laser spectra corresponding to (a), (b) and (c), respectively. The spectrum for (c) is not just the addition of (a) and (b). (e) Calculated near-field electric field distribution of the left arm in a logarithmic scale; data are taken on a plane 2 μm above the antennas. The antennas tend to direct the SP wave towards a direction perpendicular to their length, as indicated by a white arrow. (f) Enlarged view of the measured far-field pattern in (c), a black dotted circle enclose the power collection region in the polarization measurements. Noted that except for (e), all other color-coded diagrams are in linear scale.

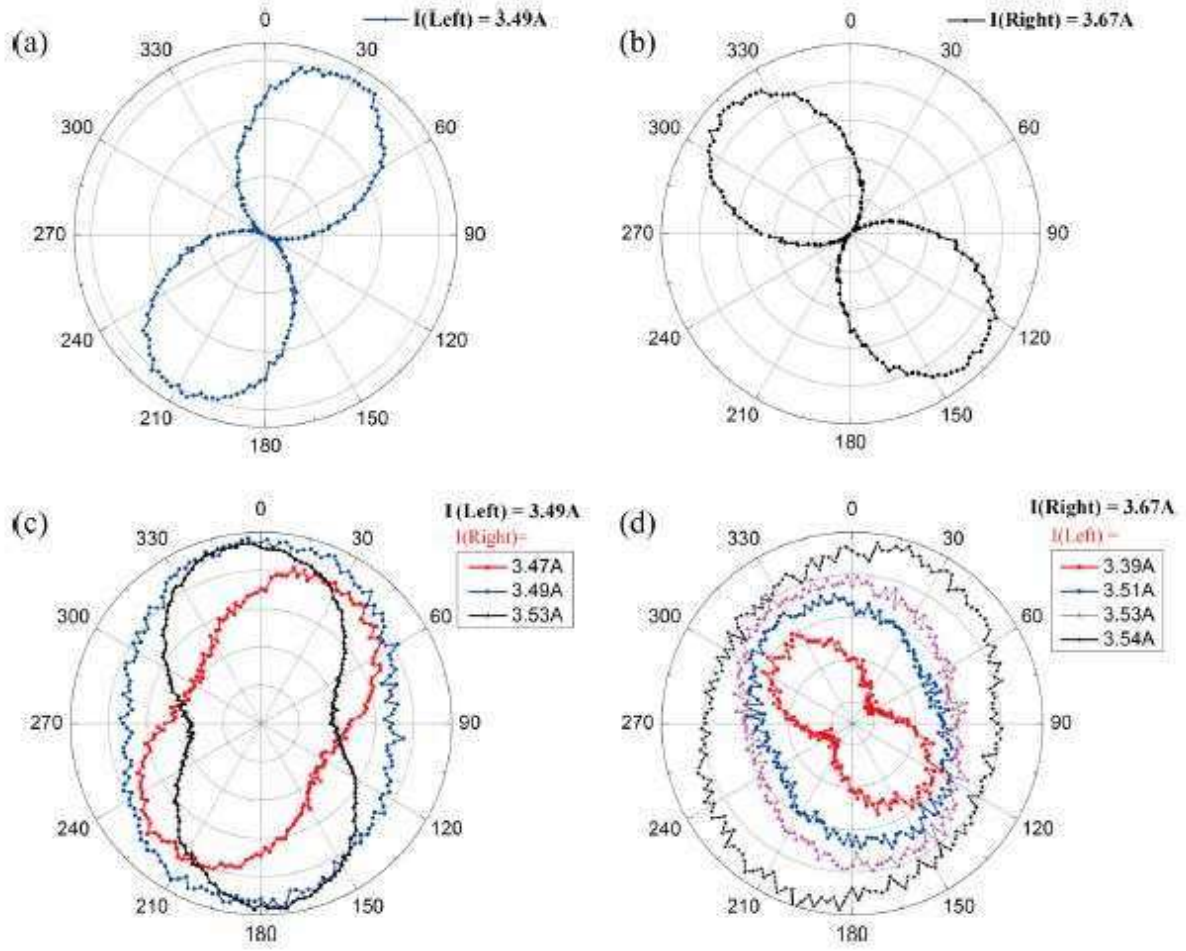

Figure 5. (a) Polarization state of the left arm of the device, measured by rotating a wire-grid polarizer in front of the detector. The power for all the measurements are collected at the intensity maximum of the far-field distribution within a half angle of 2.5°. (b) Measured polarization state of the right arm. (c) Measured polarization states with the left QCL pumped by a 3.49 A current, whilst varying the injection current to the right QCL. (d) The evolution of the polarization states when changing the injection current to the left QCL, and keeping that to the right QCL at 3.67 A. The device was demonstrated to be capable of dynamically tuning its polarization state in the power collection region from linear to near-circular, with a DOCP value as high as 99% (corresponding to the black curve in (d)).

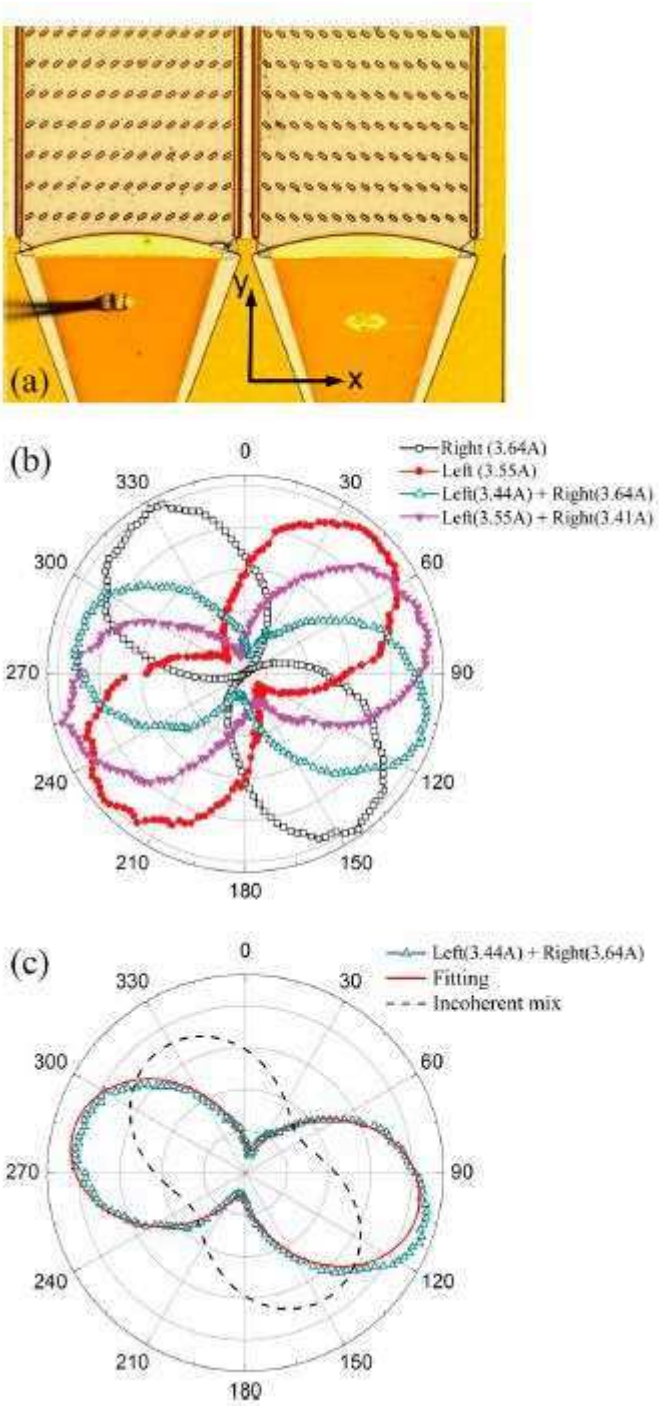

Figure 6. (a) Optical microscope image of a fabricated phase-locked device without any phase shift. (b) Measured polarization states. For the right QCL alone, the radiation in the collected region is excellently linearly-polarized at the predetermined direction, with $I_{min} \approx 0$, whilst the left QCL shows a non-negligible I_{min}. This non-zero minimum intensity from the left QCL alone can be attributed to undesired scattering of the SP wave by damage/dust on the waveguide surface. (c) Open triangles are experimental data and the red solid curve is a fitting according to coherent superimposition of the radiation from the two arms; the black dashed line is the polarization assuming incoherent mixing of the radiation from the two arms.